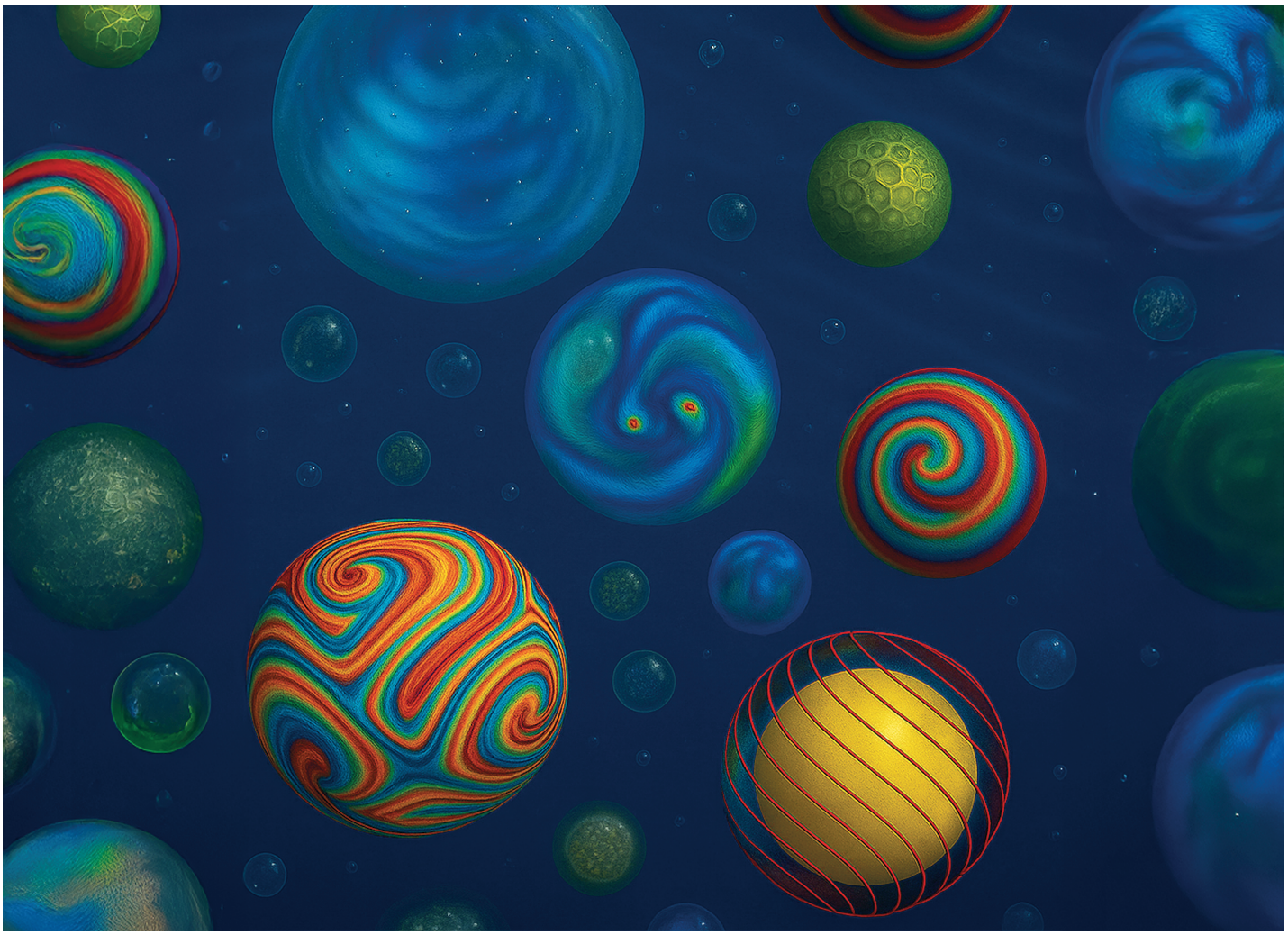

Showcasing research from Professor Sadati's laboratory, Department of Chemical Engineering, University of South Carolina, Columbia, SC 29208, United States.

Curved confinement directs anchoring-mediated structural transitions in highly chiral liquid crystal shells

In highly chiral liquid crystal shells, the interplay between confinement geometry and anchoring asymmetry governs the formation of complex mesoscale textures, such as focal conic domains and periodic stripe patterns, through pitch-axis reorientation and elastic relaxation.

Image reproduced by permission of Monirosadat Sadati from *Mol. Syst. Des. Eng.*, 2025, **10**, 836.

As featured in:

See Monirosadat Sadati *et al.*, *Mol. Syst. Des. Eng.*, 2025, **10**, 836.

ROYAL SOCIETY OF CHEMISTRY

rsc.li/molecular-engineering

Registered charity number: 207890

MSDE

PAPER

View Article Online
View Journal | View Issue

Cite this: *Mol. Syst. Des. Eng.*, 2025, 10, 836

Curved confinement directs anchoring-mediated structural transitions in highly chiral liquid crystal shells

Sepideh Norouzi,[a] Jeremy Money,[a] Stiven Villada-Gil,[b] José A. Martínez-González[c] and Monirosadat Sadati *[a]

Cholesteric liquid crystals (CLCs) confined in curved geometries exhibit a rich spectrum of defect-mediated morphologies governed by the interplay between chirality, curvature, surface anchoring, and confinement. This study systematically investigates structural transitions in highly chiral CLC shells under asymmetric anchoring conditions, focusing on the effects of shell thickness and curvature on pitch axis reorientation and defect formation. Utilizing microfluidic techniques, we generate core–shell droplets with independently tunable anchoring at inner and outer aqueous interfaces. Transitioning from planar–planar to planar-homeotropic boundary conditions *via* surfactant-mediated modulation induces profound reorganizations in the director field, giving rise to focal conic domains (FCDs), stripe patterns, and hybrid textures. Optical microscopy reveals that thicker shells favor coherent FCD nucleation, while thinner shells exhibit asymmetric, fragmented domains due to increased spatial frustration and constrained elastic relaxation. In small-diameter shells, high curvature suppresses defect nucleation, promoting the emergence of periodic stripe textures as an energetically favorable alternative. Complementary continuum simulations based on the Landau–de Gennes framework reproduce experimental trends, highlighting anchoring energy thresholds that delineate morphological regimes and confirm the dominance of curvature in stabilizing non-defect-based modulations. The ability to engineer defect architectures and direct pitch axis orientation *via* geometrical and boundary condition control can open new avenues for designing responsive and reconfigurable optical materials and photonic elements.

Received 24th April 2025,
Accepted 25th July 2025

DOI: 10.1039/d5me00070j

rsc.li/molecular-engineering

Design, System, Application

This work presents a design framework for modulating molecular orientation and defect architectures in highly chiral cholesteric liquid crystal (CLC) shells through precise control of curvature, shell thickness, and boundary anchoring. By engineering microfluidically produced CLC core–shell droplets with tunable surface interactions, we systematically explore how confinement geometry and anchoring asymmetry direct the formation of complex mesoscale textures—such as focal conic domains and periodic stripe patterns—*via* pitch-axis reorientation and elastic relaxation. The system integrates experimental characterization with continuum Landau–de Gennes simulations to uncover the energetic pathways of these transitions, providing predictive insight into the structure–function relationships governing chiral soft matter. This understanding enables the rational design of reconfigurable chiro-optical materials, soft photonic devices, and adaptive colloidal systems, where defect patterns can be leveraged to encode anisotropic responses or templated assembly. The strategy established here lays the groundwork for scalable, curvature-mediated control in responsive soft-matter platforms.

1. Introduction

Liquid crystals occupy a singular position in the landscape of soft matter—exhibiting the fluidity of liquids alongside the orientational order of crystals.[1] Found in systems as diverse as cellular membranes, viral capsids, and beetle cuticles, they are a cornerstone of biological organization.[2–5] Technologically, liquid crystals underpin modern displays and are increasingly integral to adaptive optics, photonic devices, and smart materials.[6,7] Yet, beyond their visual allure and tunable anisotropy lies a deeper, topological richness. When confined or subjected to competing boundary conditions, liquid crystals form defects—localized disruptions in their orientational order—that are not merely imperfections but carry quantized topological charge.[1] These defects, emerging from geometric frustration, encode global information about the system and

[a] *Department of Chemical Engineering, University of South Carolina, Columbia, SC 29208, USA. E-mail: sadati@cec.sc.edu*
[b] *Facultad de Ciencias y Educación, Politécnico Colombiano Jaime Isaza Cadavid, Medellín, Colombia*
[c] *Facultad de Ciencias, Universidad Autónoma de San Luis Potosí, Av. Parque Chapultepec 1570, San Luis Potosí, 78295 SLP, Mexico*

can be harnessed as active elements in material design. By exploiting their spatial positioning and interactions, researchers are now engineering defect-driven architectures for colloidal self-assembly, and responsive sensors.[8–12]

Among the various liquid crystal phases, cholesteric liquid crystals (CLCs)—or chiral nematics—are distinguished by their helical molecular organization, which emerges from the intrinsic chirality of their constituent mesogens or by adding a chiral dopant. This helicoidal arrangement, characterized by a pitch, p—the distance over which the director field, $\mathbf{n}$, completes a full rotation—gives rise to striking optical phenomena and rich topological behaviors.[1,7] When confined to curved geometries such as spherical droplets or shells, CLCs are forced to reconcile their natural helicoidal ordering with external constraints, including curvature and surface anchoring. In such systems, the orientation of the liquid crystal molecules is modulated by boundary conditions that can be either planar (tangential) or homeotropic (normal). The competition between the natural helicity of the CLC and these anchoring constraints leads to geometric frustration, which is resolved through the formation of complex textures and topological defects.

The effect of curvature and surface anchoring on the configuration of CLC has been extensively studied in droplets, especially in the low-chirality strength limit. For instance, at both low and high chirality levels, exposure of CLC droplets to phospholipids or sodium dodecyl sulfate (SDS) has been shown to trigger a transition from the Frank–Pryce planar configuration to homeotropic structures with radial helicity. This transformation gives rise to omnidirectional microlasers through Bragg-onion-type resonances, driven by multistep molecular reorientations.[13–15] These findings highlight the critical role of structural confinement in dictating the optical response of chiral liquid crystalline systems. While CLC droplets undergo complete reconfiguration at significantly lower concentrations of phospholipids than the achiral LC droplets, the low-chirality droplets detected the presence of phospholipids three times faster than their high-chirality counterparts.[13] Additionally, studies have demonstrated that adjusting the droplet size and pitch of CLCs—*via* microfluidic control and dopant concentration, respectively—in droplets with weak planar surface anchoring can stabilize either a single helical structure or a double-twisted configuration.[16] Altering p in droplets with strong degenerate planar anchoring, alternatively, can reconfigure the chiral droplets from a twisted bipolar structure to a radial spherical arrangement.[17] Upon transition from degenerate planar to homeotropic anchoring, on the other hand, chiral droplets undergo a substantial rearrangement, forming structures reminiscent of 2D skyrmions.[18]

Confining CLC within spherical shells, where positive and negative Gaussian curvatures coexist, has significantly deepened our understanding of how curvature governs structural stability and the formation of topological defects. The spherical shell geometry serves as a powerful platform to dissect the competing roles of bulk elastic energy, geometrical confinement, and surface anchoring. For example, planar-aligned chiral shells have been shown to exhibit radial spherical structures (RSS) featuring intertwined defect lines, which transition into focal conic domains (FCDs) under homeotropic anchoring conditions.[19,20] In Janus-type CLC shells, low-chirality systems can support diverse configurations such as cholesteric fingers and skyrmions, whose stability and morphology can be modulated by tuning surface boundary conditions or applying external fields.[21] These spatially dynamic, reconfigurable patterns in chiral shells offer a promising route to engineering functional colloidal architectures and chiro-optical devices.[22–24]

In addition to anchoring conditions, two geometrical parameters play a pivotal role in determining the equilibrium and metastable structures in cholesteric shells: shell thickness and curvature. Shell thickness, h, typically normalized by the CLC pitch (h/p), determines the number of helical layers that can fit between the inner and outer boundaries. Curvature adds another layer of complexity. Because the inner and outer surfaces of the shell have opposing Gaussian curvatures, the energy landscape for defect formation becomes asymmetric. Convex surfaces, such as the outer shell boundary, tend to stabilize focal conic structures more readily than concave inner surfaces, where curvature resists the necessary deformation of cholesteric layers.[25]

Darmon *et al.* developed a theoretical model describing elastic interactions in cholesteric shells and showed how thickness heterogeneity drives the self-positioning of topological defects. Their work also emphasized the nontrivial nature of disclination lines in chiral systems, where classical nematic defect theories often fail. Tran *et al.* have made significant contributions by systematically studying anchoring transitions in CLC shells. Their work revealed that intermediate anchoring conditions, achievable through surfactant modulation or thermal treatment, give rise to a rich variety of stripe patterns and defect configurations.[20] Despite these advances, most studies have focused on CLCs with low chirality (*i.e.*, large p), leaving the behavior of highly chiral systems largely unexplored. Notably, Norouzi *et al.* recently extended this investigation to highly chiral CLCs ($p < 300$ nm), where upon heating, the system undergoes a transition to intermediate self-assembled blue phases prior to reaching the isotropic state.[25,26] Their findings revealed pronounced effects of both confinement (shell thickness) and curvature (droplet size) on CLC configurations and structural transitions under varying anchoring conditions. While these works highlight that the interplay among confinement, curvature, and boundary anchoring governs whether the director field remains planar, bends, or reorients, a comprehensive and systematic study of the effect of curvature and shell thickness on the transitional regimes and the associated defect dynamics remain unexplored. Moreover, the interplay between pitch axis reorientation, defect stabilization, and the energetic pathways of structural transitions in such highly chiral systems has yet to be investigated. This study aims to fill this gap by exploring the

structural transitions that occur as the shell morphology evolves from planar–planar to planar-homeotropic boundary conditions in highly chiral CLC shells.

By systematically varying curvature and confinement, we map out the resulting textures and identify structural transitions, defect formation, and pitch axis reorientation. Through a combination of experimental observations and computational simulations, we seek to unravel the geometric and topological mechanisms that govern these transitions. Understanding these transitions is essential not only for advancing the fundamental physics of liquid crystals but also for enabling their integration into tunable optical elements, responsive emulsions, and bio-inspired materials.

2. Materials and methods

2.1. Experiments

To prepare highly chiral cholesteric mixtures, 37 wt% of the chiral dopant S811 (2-octyl 4-(4-hexyloxybenzoyloxy)benzoate; Merck) was combined with 63 wt% of the nematic host MLC2142 (1-methyl-4-(4-*trans*-vinyl-[1,1′-bicyclohexyl]-4′-*trans*-yl)-benzene, EMD Chemicals). Toluene was used as a co-solvent to dissolve the mixture and subsequently evaporated under reduced pressure using a rotary evaporator to ensure the mixture's homogeneity. The pitch length, p, is inversely proportional to the concentration of the chiral dopant and is defined by the relation $p = 1/(c \times \mathrm{HTP})$, where c is the dopant concentration and HTP denotes the helical twisting power.[27] Thereby, for the chiral dopant S-811, which has a reported HTP of 10.9 μm^{-1}, the resulting p was calculated to be approximately 250 nm. To control surface anchoring at the aqueous–liquid crystal interface, polyvinyl alcohol (PVA, MW 13–23 K, 87–89% hydrolyzed; Sigma-Aldrich) and sodium dodecyl sulfate (SDS, >98% purity; Sigma-Aldrich) were added to the aqueous phases. Shell thickness was modulated *via* osmotic thinning by adding sodium chloride (NaCl; Sigma-Aldrich) and glycerol (Acros Organics) to the aqueous phases. To facilitate wetting control, the inner surfaces of glass capillaries were chemically functionalized using either 2-[methoxy(polyethyleneoxy)propyl]trimethoxysilane (Gelest) for hydrophilicity or dimethyloctadecyl[3-(trimethoxysilyl) propyl]ammonium chloride (DMOAP, 72% purity; Sigma-Aldrich) for hydrophobicity.

CLC core–shell droplets were generated using a custom microfluidic device with combined co-flow and flow-focusing geometries (Fig. 1A and B), adapted from the design of Utada *et al.*[28] Two cylindrical borosilicate glass capillaries (0.58 mm ID, 1.0 mm OD; WPI) were pulled using a micropipette puller (P-2000, Sutter Instrument, US) and fire-polished with a Microforge (MF-900, Narishige, Japan) to precisely adjust their openings. The tapered injection and collection capillaries were aligned concentrically inside a square capillary (1.05 mm ID, 1.50 mm OD; Harvard Apparatus), separated by 300 μm, and fixed onto a glass slide. The injection capillary was rendered hydrophobic using a 1 wt% DMOAP solution, while the collection and square capillaries were treated with polyethyleneoxy silane to ensure hydrophilicity. Fluid injection was controlled *via* three syringe pumps (Elite 11 series, Harvard Apparatus), set to flow rates of 200 μL h^{-1} (inner aqueous phase), 100 μL h^{-1} (CLC phase), and 4000 μL h^{-1} (outer aqueous phase).

In the microfluidic setup, the inner aqueous phase was introduced through the hydrophobic injection capillary, while the CLC phase flowed in the annular space between the injection and square capillaries. The outer aqueous phase, injected through the surrounding region between the square and collection capillaries, served as the continuous phase, flow-focusing the inner and middle fluids. This geometry allowed the formation of core–shell droplets, where the aqueous core was encapsulated by a thin liquid crystal shell and suspended within the outer aqueous environment (Fig. 1C).[25]

The alignment of the CLC shell at each aqueous interface was tuned independently using surfactant-containing water–glycerol solutions (80 : 20 v/v). Hybrid anchoring configurations were achieved by employing PVA and SDS surfactants in the inner and outer aqueous phases,

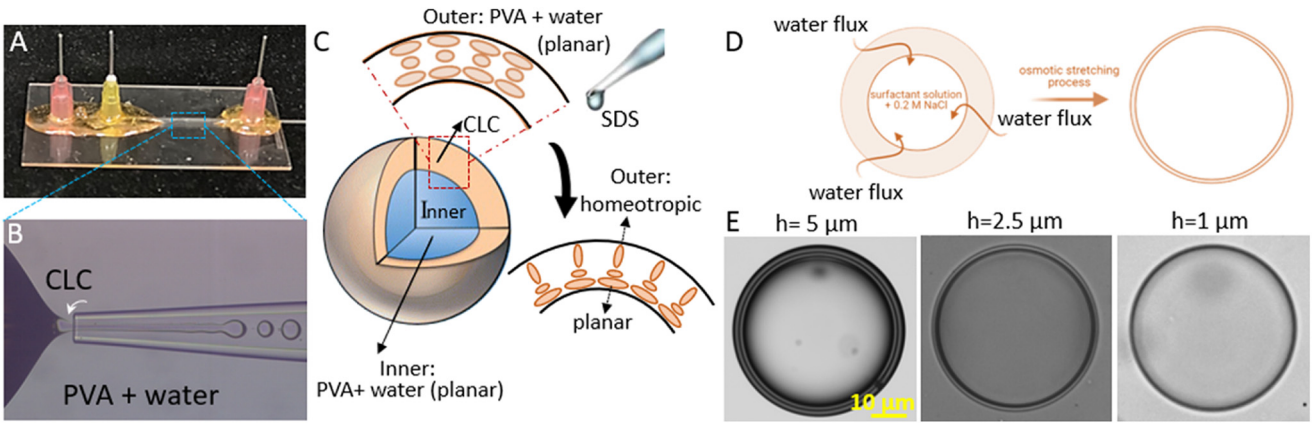

Fig. 1 (A and B) microfluidic setup and core–shell droplet generation. (C) Illustration of a CLC core–shell droplet with planar–planar anchoring and its transition to planar-homeotropic anchoring upon addition of SDS to the outer interface. (D) Schematic representation of the osmotic thinning process, and (E) bright-field micrographs of CLC shells at varying shell thicknesses.

respectively (Fig. 1C). PVA induces degenerate planar surface anchoring compelling chiral molecules to align tangentially at the aqueous interface, orienting the helical twist axis perpendicular to the surface without introducing elastic frustration (Fig. 1C). This configuration results in a radial structure that appears as a characteristic cross pattern under polarized optical microscopy. In contrast, homeotropic anchoring enforces perpendicular alignment of the molecules to the interface, thereby orienting the twist axis parallel to the surface—an arrangement that conflicts with the preferred perpendicular twist axis orientation observed in the bulk phase (Fig. 1C). To further reduce shell thickness, an osmotic pressure gradient was imposed by dissolving 0.2 M NaCl in the inner aqueous phase, producing an approximate osmolarity difference of 0.98 osmol L^{-1} (Fig. 1D and E).[29]

Core–shell droplets were imaged using a Zeiss Axioscope X5 microscope (Zeiss, Oberkochen, Germany) under both bright-field and crossed-polarized reflection modes using a 50× objective. For optical characterization, samples were collected in lab-fabricated cells consisting of two no. 1 coverslips separated by a 100 μm-thick polydimethylsiloxane (PDMS) spacer ring.

2.2. Continuum simulations

A continuum mean field Landau–de Gennes formalism was used to model the free energy, F, of a CLC within a shell confinement.[30,31] In this approach, the free energy is a function of the tensor order parameter, $\boldsymbol{Q}$, defined by $\boldsymbol{Q}_{ij} = S(n_i n_j - 1/3\delta_{ij})$, with $i, j = 1, 2, 3$, and n_i are the x, y, z components of the local director vector, S is the scalar order parameter, given as $S = <3/2\cos^2\theta - 1/2>$, with $\cos\theta = a{\cdot}n$, where a is the molecular orientation and $<>$ denotes a spatial average. Thus,

$$F(\boldsymbol{Q}) = \int d^3x[f_P(\boldsymbol{Q}) + f_E(\boldsymbol{Q})] + \int d^2x f_S(\boldsymbol{Q}), \quad (1)$$

where f_P accounts for the short-range contribution, while f_E accounts for the elastic long-range contribution, and f_S corresponds to the surface contribution to the free energy. The phase free energy density is given by,

$$f_P = \frac{A}{2}\left(1 - \frac{U}{3}\right)\mathrm{tr}(\boldsymbol{Q}^2) - \frac{AU}{3}\mathrm{tr}(\boldsymbol{Q}^3) + \frac{AU}{4}\mathrm{tr}(\boldsymbol{Q}^2)^2. \quad (2)$$

where A and U are phenomenological parameters that depend on temperature and pressure. The elastic free energy density is given by,

$$f_E = \frac{L}{2}\left[\frac{\partial \boldsymbol{Q}_{ij}}{\partial x_k}\frac{\partial \boldsymbol{Q}_{ij}}{\partial x_k} + 4q_0\varepsilon_{ikl}\boldsymbol{Q}_{ij}\frac{\partial \boldsymbol{Q}_{lj}}{\partial x_k}\right], \quad (3)$$

where $q_0 = 2\pi/p$ is the inverse of the pitch (p), L presents elastic constants, and ε_{ikl} is the Levi-Civita tensor. It is worth noting that, within the Landau–de Gennes (LdG) framework, the chiral contribution to the elastic free energy can be expressed in two mathematically equivalent forms. The first, which we adopt here (eqn (3)), is an explicit linear coupling term that is commonly used in simulations of cholesteric systems.[19,32,33] The second is a square form $L/2[\varepsilon_{\alpha\gamma\delta}\partial_\gamma \boldsymbol{Q}_{\delta\beta} + 2q_0\boldsymbol{Q}_{\alpha\beta}]^2$, which has also been employed in the literature.[20,34] As discussed by Hicks and Walker,[37] the alternative formulation differs only by an additional term proportional to $q_0{}^2\mathrm{tr}(\boldsymbol{Q}^2)$, which can be merged into the bulk free energy without altering the system's qualitative behavior. Following standard practice, we adopt the explicit linear form of the chiral coupling term to keep it separate from the thermodynamic potential. This allows for a clearer distinction between elastic and bulk contributions and preserves the effective phase behavior of the scalar order parameter.

In this work, we employ the widely used one-elastic-constant approximation and neglect the saddle-splay contribution, a simplification commonly used when modeling generic features of CLCs—especially in systems where twist deformation dominates due to strong chirality and surface anchoring.[32,35] Given the small intrinsic pitch and strong anchoring in our system, twist distortion emerges as the dominant elastic mode. The one-constant approximation thus captures the essential physics while reducing computational complexity.

Excluding the saddle-splay term also avoids additional $\mathrm{tr}(\boldsymbol{Q}^2)$ contributions to the elastic energy, which could otherwise shift the effective bulk phase diagram. This modeling approach ensures a consistent separation between elastic and thermodynamic contributions and preserves the central role of chirality in the formation of twisted textures.

The last term of eqn (1) corresponds to the surface contributions to the free energy. For a shell geometry, we must consider two independent (inner and outer) surfaces. In this work, we first imposed planar degenerate anchoring conditions on both surfaces, where the surface free energy density is,[36]

$$f_S^P = W_P(\tilde{\boldsymbol{Q}} - \tilde{\boldsymbol{Q}}^\perp)^2, \quad (4)$$

where W_P is the anchoring strength, $\tilde{\boldsymbol{Q}} = \boldsymbol{Q} + S\boldsymbol{I}/3$ and $\tilde{\boldsymbol{Q}}^\perp = \boldsymbol{P}\tilde{\boldsymbol{Q}}\boldsymbol{P}$. The projection operator is defined by $P_{ij} = \delta_{ij} - \mathbf{v}_i\mathbf{v}_j$, where $\mathbf{v}$ is the vector normal to the surface. To study how a change at the anchoring condition triggers a reconfiguration of the CLC morphology, we also consider homeotropic anchoring conditions for the outer shell surface. The surface free energy associated with the homeotropic anchoring is given by,

$$f_S^H = \frac{1}{2}W_H(\boldsymbol{Q} - \boldsymbol{Q}^0)^2, \quad (5)$$

where W_H is the homeotropic anchoring energy and $\boldsymbol{Q}^0$ is the preferred surface tensor order parameter.

For a given initial condition set by an initial $\boldsymbol{Q}$-tensor, the minimization of the free energy is achieved using the Ginzburg–Landau relaxation method, where $\boldsymbol{Q}$ evolves toward equilibrium according to,[30]

$$\frac{\partial \boldsymbol{Q}}{\partial t} = -\frac{1}{\gamma}\left[\boldsymbol{\Pi}\left(\frac{\delta F}{\delta \boldsymbol{Q}}\right)\right], \quad (6)$$

with boundary conditions, such that $\boldsymbol{\Pi}[(\delta F/\delta\nabla\boldsymbol{Q})\cdot\boldsymbol{\nu}] = 0$, where $\boldsymbol{\Pi}(\boldsymbol{B}) = 1/2(\boldsymbol{B} + \boldsymbol{B}^T) - 1/(3\mathrm{tr}(\boldsymbol{B})\boldsymbol{I})$ ensures the symmetric and

traceless properties of the $\boldsymbol{Q}$-tensor parameter, and γ is a diffusion coefficient. The minimization of the free energy functional for CLC shells with a diameter of approximately 2 μm was performed using the finite difference method. A lattice array was implemented with a mesh resolution equal to the coherence length, defined as $\xi_C = \sqrt{L/A} \approx 7.5$ nm. Unless otherwise specified, we used reported values for the anchoring energies, *i.e.*, $W_P = W_H = 1 \times 10^{-3}$ J m^{-2}, and phenomenological parameters characteristic of a CLC: $A = 1.067 \times 10^5$ J m^{-3}, $L = 6$ pN, a chiral pitch of 250 nm, and a thermal parameter $U = 5$, which corresponds to a bulk scalar order parameter $S \approx 0.76$, based on the expression $S_{bulk} = 1/4 + 3/4\sqrt{1 - \frac{8}{3}U}$. To nondimensionalize the problem, we used the elastic constant L, the coherence length ξ_C, and the extrapolation length $\xi_s = L/W$ to define the reduced variables: $r^* = r\xi_c^{-1}$, $F^* = FL^{-1}\xi_c^{-1}$ and $W^* = \xi_c\xi_s^{-1}$.

3. Results and discussions

3.1. Anchoring-induced transition

Using a PVA-water solution, all core–shells were originally prepared having planar–planar anchoring on inner and outer shell–aqueous interfaces (Fig. 1C). The outer surface properties were adjusted to homeotropic anchoring by adding SDS into the aqueous medium (10 mM) (Fig. 1C). Fig. 2 illustrates the dynamic reorganization of director configurations within a highly chiral core–shell droplet (70 μm diameter) with the largest shell thickness studied (5 μm), in response to anchoring modulation. Initially, the system exhibits planar anchoring at both the inner and outer interfaces, yielding an onion-like RSS characteristic of the Frank–Pryce texture (Fig. 2ii). This structure is defined by concentric cholesteric layers aligned tangentially to both boundaries, creating a well-ordered, optically reflective shell that embodies the helicoidal architecture of the CLC (Fig. 2ii).

Upon the introduction of SDS into the surrounding aqueous medium, a transition is initiated at the outer surface, changing the anchoring from planar to homeotropic. The transition from planar–planar to planar-homeotropic anchoring breaks the radial continuity of the cholesteric layers and induces a reorientation of the pitch axis. The incompatibility between the natural cholesteric twist and the enforced boundary conditions at the outer surface introduces geometric frustration, which is relieved through the nucleation of FCDs as stable, energy-minimizing structures capable of accommodating the elastic strain induced by the conflicting anchoring preferences. These domains first appear as localized distortions on the outer surface and progressively expand over time (Fig. 2iii–v, Movie S1). The growth of these domains proceeds *via* lateral expansion and coalescence, eventually covering the entire outer shell surface (Fig. 2v). Transition to homeotropic anchoring and the development of out-of-plane focal conic structures lead to surface roughness on CLC shells, evolving from an initially smooth planar interface. These deformations are readily observable using standard optical microscopy (Fig. 2i and vi).

Reducing the shell thickness from 5 μm to 2.5 μm while maintaining the same droplet diameter significantly alters the pathway and morphology of the anchoring-induced

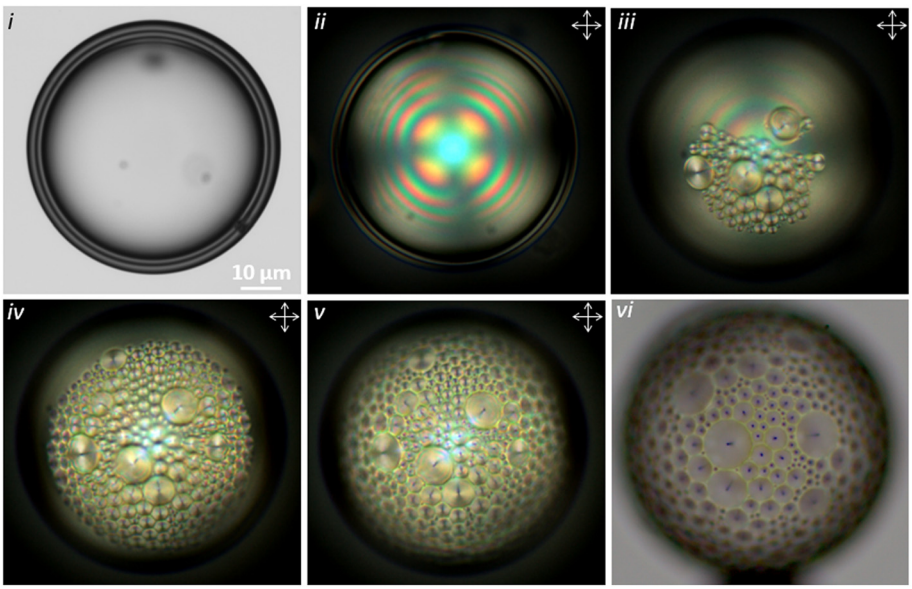

Fig. 2 Anchoring-induced transition from a planar–planar RSS configuration (ii) to planar-homeotropic alignment (v), accompanied by FCD nucleation and growth, in a CLC shell with a diameter of 70 μm and shell thickness of 5 μm. Panels i and ii display the bright-field and reflection-mode cross-polarized micrographs, respectively, of the core–shell droplet before SDS addition. Panels iii–v show reflection-mode cross-polarized images captured at t = 180, 270, and 360 seconds after SDS was introduced, representing gradual transitions of RSS to focal conics configuration. Panel vi presents the bright-field image of focal conic domains.

structural transition (Fig. 3, Movie S2). While FCDs still nucleate and expand following SDS addition, they appear less uniform, exhibiting pronounced asymmetry and irregularity in size and orientation (Fig. 3iv–vi). This behavior can be attributed to the drastically reduced confinement ratio (h/p), which limits the number of cholesteric layers that can accommodate the transition-induced deformation. In such a regime, the elastic energy landscape becomes dominated by sharp pitch gradients and incomplete relaxation of twist and bend deformations. As a result, rather than reorganizing into coherent, symmetric domains as in thicker shells, the system fractures into smaller, defect-laden regions that lack a global registry (Fig. 3v and vi). The spatial disorder and interrupted domain growth suggest that elastic compatibility between inner planar and outer homeotropic anchoring becomes more difficult to resolve with decreasing thickness, leading to a frustration-dominated state.

Notably, this irregular propagation of FCDs supports the hypothesis that there exists a critical threshold below which coherent pitch-axis reorientation cannot proceed smoothly. Instead, the shell stabilizes metastable textures whose morphology reflects the local accommodation of strain rather than global energetic minimization.

Confinement-induced asymmetry: disrupted FCD morphologies in ultra-thin cholesteric shells. In ultra-thin shells with a thickness of only 1 μm, the transition from planar–planar to planar-homeotropic anchoring produces an intricate interplay of competing textures and defect motifs (Fig. 4). While FCDs appear as expected under the influence of SDS-induced homeotropic anchoring at the outer interface, the structural changes initiate with the emergence of stripe patterns (Fig. 4iii–vi), resulting in a hybrid morphology that significantly deviates from the patterns observed in thicker shells (Movie S3). Here, the limited spatial extent of the cholesteric layers inhibits continuous domain expansion, leading to the co-existence of both irregular FCDs and stripe-like textures distributed across the shell surface (Fig. 4vi).

The FCDs appear highly asymmetric and fragmented, and their morphology lacks the radial coherence characteristic of larger domains observed in thicker shells (Fig. 4vi and 2v), highlighting the impact of spatial frustration in thin geometries. Concurrently, cholesteric stripes form adjacent to or interwoven with these domains, often exhibiting local discontinuities, which indicate a lack of long-range ordering. This hybrid texturing reflects a complex compromise between the system's intrinsic tendency to form layered helicoidal structures and the imposed anchoring asymmetry. The shell's ultra-thin geometry restricts the number of full helical turns that can be accommodated between the inner and outer surfaces, forcing the director to reorient sharply and non-uniformly across the thickness. As a result, the pitch axis becomes highly distorted, generating conditions that favor both layer bending (associated with FCDs) and compression (underlying stripe formation).

The stripe textures, characterized by periodic banding, are understood as the manifestation of a pitch axis aligned preferentially parallel to the surface, stabilized under moderate homeotropic anchoring and high curvature. These

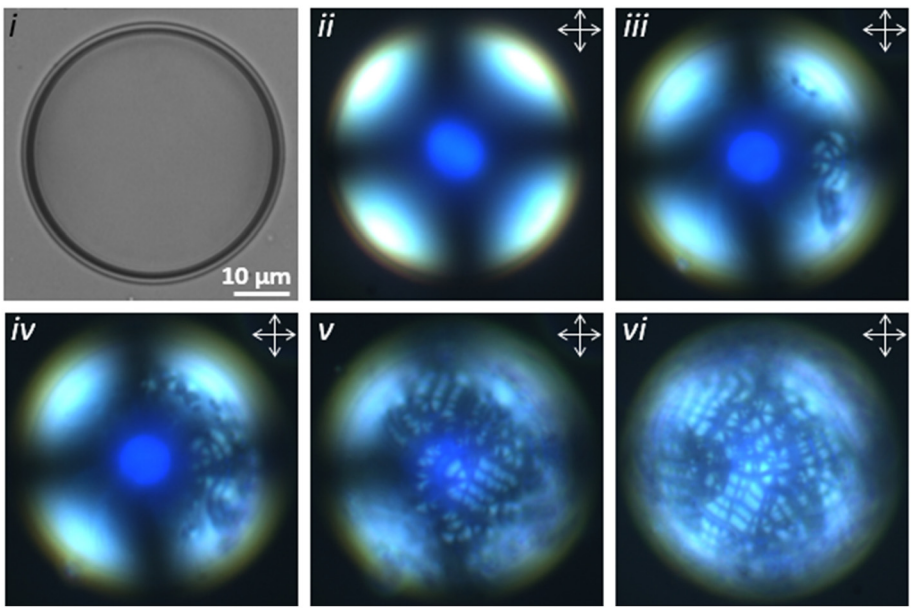

Fig. 3 Anchoring-induced transition from planar–planar RSS configuration (ii) to planar-homeotropic alignment (vi) in a CLC shell with a shell thickness of 2.5 μm accompanied by disrupted FCD nucleation and growth. Panels i and ii display the bright-field and reflection-mode cross-polarized micrographs, respectively, of the core–shell droplet prior to SDS addition. Panels iii–vi show reflection-mode cross-polarized images captured at t = 180, 210, 270, and 360 seconds after SDS was introduced, representing gradual transitions of RSS to focal conics with fine and irregular structure.

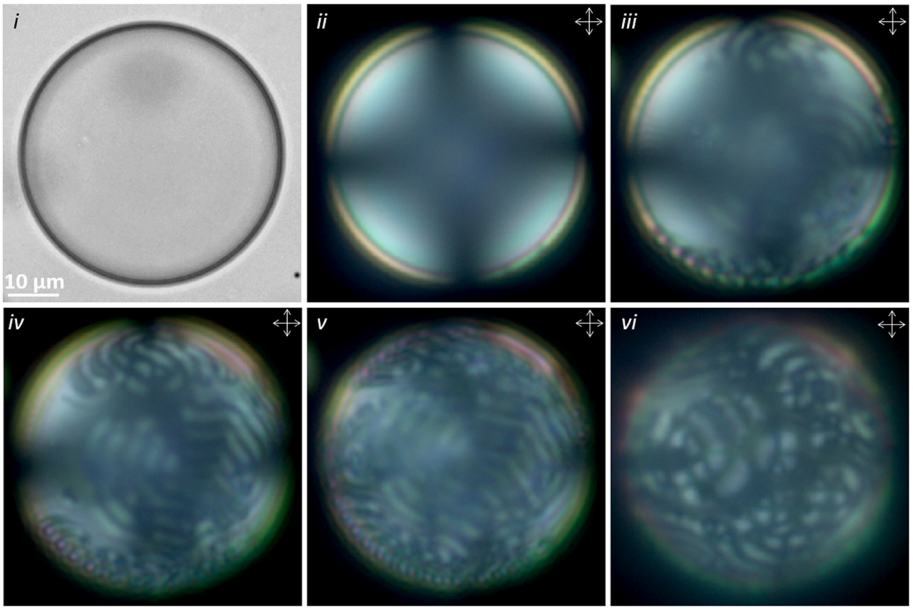

Fig. 4 Coexistence of FCDs and stripe patterns in an ultra-thin (1 μm), highly chiral CLC shell undergoing an anchoring-induced transition from a planar–planar RSS configuration to planar-homeotropic alignment. Panels i and ii display the bright-field and reflection-mode cross-polarized micrographs, respectively, of the core–shell droplet prior to SDS addition. Panels iii–vi demonstrate reflection-mode cross-polarized images captured at t = 180, 210, 240, and 260 seconds after SDS was introduced, representing the gradual transition of RSS to a hybrid focal conic-stripe pattern configuration.

patterns grow laterally without forming singular defects, unlike FCDs, and may represent a metastable intermediate between fully bent and planar cholesteric layering. Their presence alongside FCDs implies competition between two distinct elastic relaxation pathways, likely modulated by local variations in shell thickness.

Additionally, comparative analysis with thicker shells (Fig. 2v and 3vi) reveals that shell thickness not only plays a key role in the energetics of cholesteric layer rearrangement and the topology of emergent patterns but also dictates the kinetics of structural transitions and defect formation. Thinner shells exhibit substantially faster

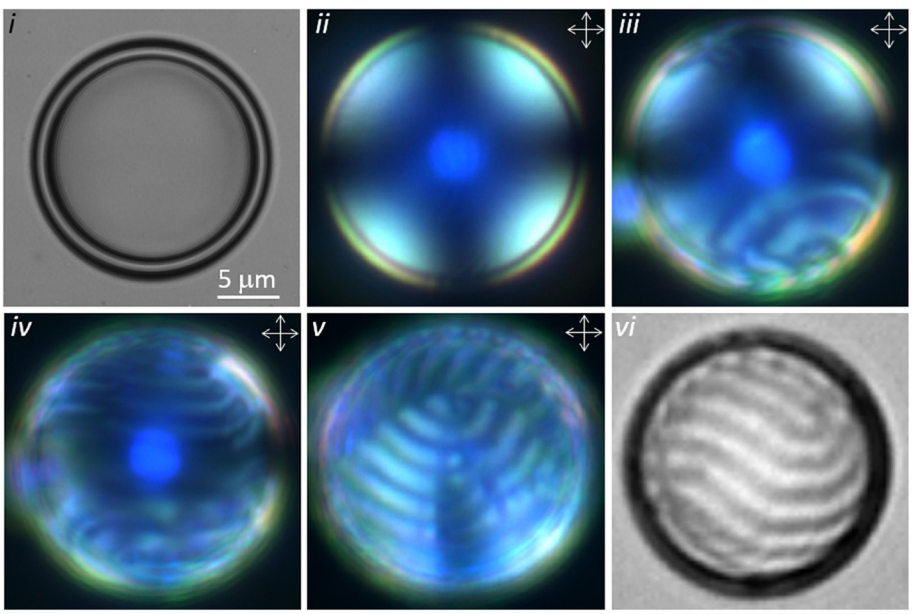

Fig. 5 Anchoring-induced transition from a planar–planar RSS configuration to planar-homeotropic alignment in a CLC shell with a diameter of 20 μm and a shell thickness of 2.5 μm. Panels i and ii display the bright-field and reflection-mode cross-polarized micrographs, respectively, of the core–shell droplet prior to SDS addition. Panels iii–v present reflection-mode cross-polarized images taken at t = 120, 145, and 190 seconds after SDS addition, illustrating the complete transition of the RSS structure into a stripe pattern configuration without the formation of focal conic structures. Panel vi presents a bright-field image of stripe patterns formed on the core–shell droplet.

reconfiguration dynamics (Fig. 4vi), demonstrating the critical role of geometric confinement in directing cholesteric ordering.

3.2. Curvature-induced stripe stabilization in small-diameter chiral shells with asymmetric anchoring

Reducing the overall droplet diameter to 20 μm while maintaining a shell thickness of 2.5 μm introduces a distinct confinement regime, where increased curvature and reduced volume-to-surface ratio amplify the influence of boundary anchoring (Fig. 5). Under initial planar–planar conditions, the CLC shell exhibits a RSS configuration, consistent with a concentric Frank–Pryce texture (Fig. 5ii). However, upon the introduction of SDS to the outer aqueous phase, which promotes homeotropic anchoring, a clear transition emerges. Rather than nucleating FCDs, the system develops a well-defined stripe texture across the outer shell surface, indicative of pitch axis reorientation under asymmetric boundary conditions (Fig. 5iii, Movie S4).

This pronounced change in morphology with respect to similarly thick but larger droplets elucidates the critical role of curvature in modulating defect formation pathways and layer orientation. In this highly curved geometry, the outer shell surface exerts stronger constraints on the cholesteric pitch axis, driving it to align tangentially to the shell surface in regions of high curvature. As a result, periodic modulations of the director field emerge along the surface, forming stripes that reflect a quasi-planar alignment constrained by the local topology and anchoring asymmetry.

The emergence of stripes in the absence of FCDs distinguishes this configuration from larger droplets or thicker shells, where FCDs readily nucleate to relieve frustration. Here, the smaller radius of curvature enhances the energetic penalty associated with bending cholesteric layers into defect-rich domains. Consequently, the system adopts a different relaxation pathway, redistributing elastic stress through periodic layer compression and pitch axis tilting, which manifest as stripe patterns. Their coherent yet curvature-adapted growth suggests that curvature not only frustrates layer alignment but also stabilizes non-defect-based modulations. Compared to thicker or larger systems, the stripe domains here are more uniform and continuous, with fewer signs of kinetic trapping or defect pinning, implying the stripe formation may represent the thermodynamically favored state. Moreover, a higher degree of curvature, in particular, exhibits significantly accelerated reconfiguration dynamics compared to droplets of similar thickness with lower curvature (Fig. 3), emphasizing the strong influence of the curvature of the confining boundary on the self-organization behavior of cholesteric liquid crystal shells.

To gain insights into the director field morphology during CLC reconfiguration in small droplets, we conducted continuum simulations based on the Landau–de Gennes framework. These simulations explored changes in anchoring conditions and their effects. Specifically, we examined shells with planar degenerate anchoring on both inner and outer surfaces, which exhibit a stable RSS at room temperature. We achieved this phase in our simulations by initializing the director field with RSS ansatzes for the $\boldsymbol{Q}$-tensor[37] *i.e.*,

$$\boldsymbol{n}(r, \phi, \theta) = \cos \Omega \mathbf{e}_\theta + \sin \Omega \mathbf{e}_\phi, \quad (7)$$

where $\Omega = \phi + q_0 r$, while $\mathbf{e}_\theta$ and $\mathbf{e}_\phi$ are the unit vector in spherical coordinates. Once the CLC confined in the shell equilibrates in an RSS, we changed the anchoring conditions of the outer surface of the shell. We did this in two different ways as follows.

In the first approach, we modified the outer surface anchoring to homeotropic and stored the out-of-equilibrium $\boldsymbol{Q}$-tensor at various simulation steps until the free energy difference between consecutive iterations met the criterion $\Delta F^* < 10^{-7}$. This approach enabled us to gain insight into the system's evolution in response to a sudden change in anchoring conditions from planar to homeotropic. Fig. 6A illustrates the CLC configuration at different stages, starting from the stable RSS. Upon switching to homeotropic anchoring, the RSS becomes unstable, and the CLC begins to equilibrate towards a stripe configuration. Previous studies by Lavrentovich *et al.* have shown that interfacial changes in anchoring conditions can induce Helfrich–Hurault-like instabilities. These arise when the pitch axis tilts near curved interfaces due to anchoring incompatibilities, generating elastic strain that relaxes *via* periodic modulations of the cholesteric layers, typically with a wavelength around twice the intrinsic pitch.[38] In our simulated structures, this intermediate configuration is also seen during the director's reorientation near the surface because of the anchoring change. The abrupt transition from planar to homeotropic anchoring induces a degenerate tilt in the pitch-axis direction $\vec{p}$. In the initial RSS state, $\vec{p}$ is radial and tilts without a preferred orientation as depicted by the black arrows in Fig. 6A. Since there is no preferred direction for this reorientation, as the system evolves, the resulting stripes appear disordered,[38] as illustrated in Fig. 6A for the cases $\Delta f^* = 1$ and 10^{-3}. Note that Δf^* is the free energy density difference between two consecutive simulation cycles, which vanishes as the system approaches equilibrium. Finally, the strong homeotropic anchoring forces $\vec{p}$ to be tangential to the interface, and the minimum free energy configuration corresponds to an aligned stripe configuration (as shown for $\Delta f^* < 10^{-7}$ in our simulations). Additionally, since we are considering strong anchoring conditions, the CLC is forced to unwind near the outer homeotropic interface, producing the line defects shown in Fig. 6. During RSS-stripe pattern transition, FCDs also emerge, particularly in larger droplets, characterized by double spirals in the director field at the shell surface (Fig. 6B).

Although our previous work[25] examined the effect of droplet size on the final configuration of CLC shells at a confinement ratio of $h/p = 2$ (h is the shell thickness and p is

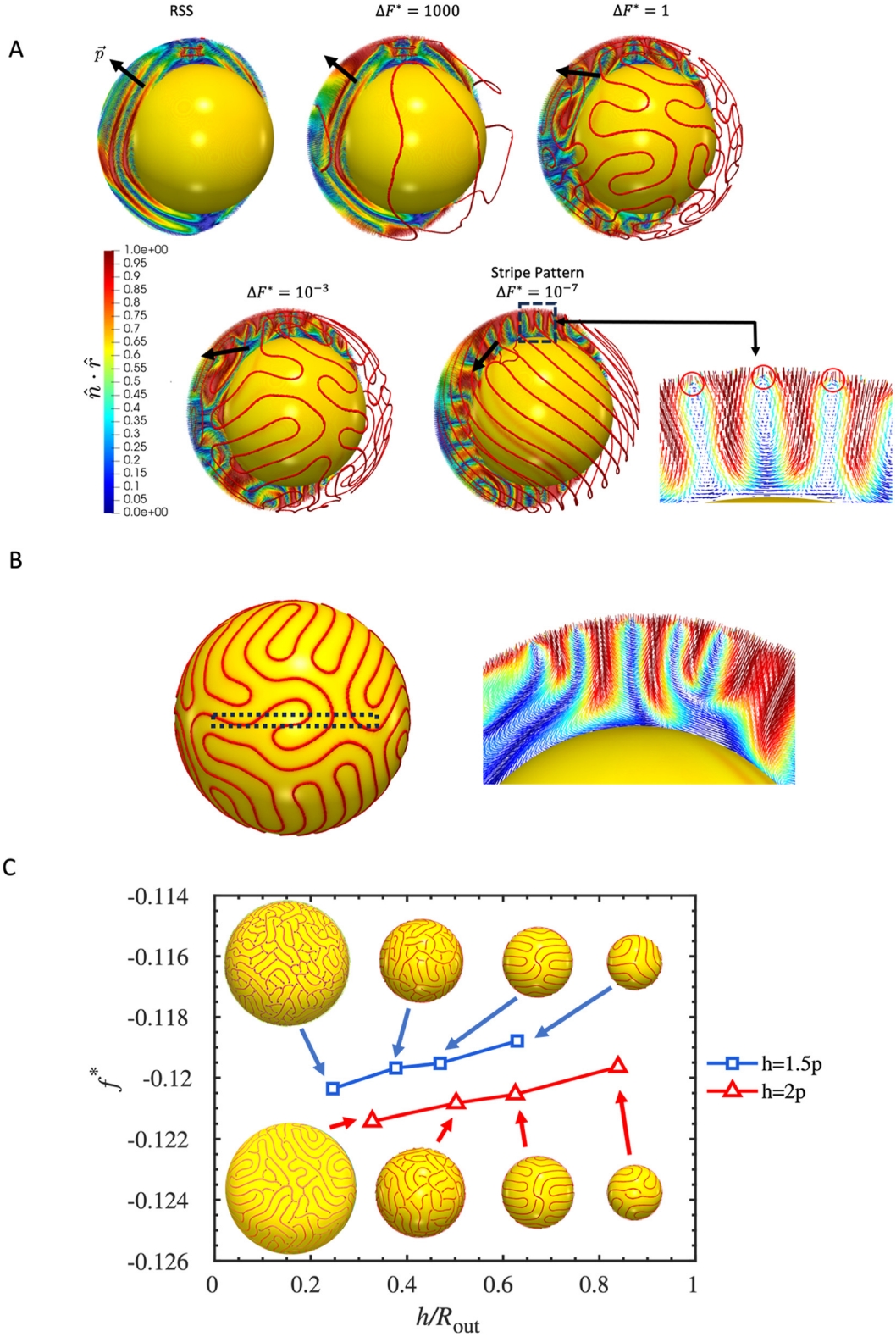

Fig. 6 Simulation results for the anchoring-induced transition from RSS to the stripe pattern for shells. The initial condition of the simulations corresponds to the RSS, which is imposed by the planar–planar anchoring conditions; the anchoring of the outer surface is then changed to homeotropic. A) The figure shows the reconfiguration of the director field as the system equilibrates to the new anchoring conditions. Equilibration is assumed when there is not a significant change in the free energy of the system as a function of the simulation time. B) Coexistence of stripe patterns and double-spiral (FCD structures) configurations, accompanied by a director field snapshot highlighting the selected region containing the double-spiral structure. For A and B, droplet diameter D = 2 μm, confinement ratio $\frac{h}{p} = 1.0$, and the color map of the director field goes from blue to red depending on the radial projection of the directors ($\hat{n}\cdot\hat{r}$). C) Free energy density as a function of h/R_{out}, demonstrating a transition from stripe pattern (thin shells) to a hybrid structure (thicker shells). In all cases, the disclination lines are visualized as isosurfaces of the scalar order parameter S = 0.45 shown in red.

the pitch length), here we extend our simulations to include additional shell thicknesses beyond those previously explored, allowing a more comprehensive investigation of how the confinement ratio and curvature govern structural outcomes and supports the construction of a detailed phase diagram. As shown in Fig. 6C, larger droplets tend to support hybrid textures, whereas smaller droplets exhibit higher free energy densities, favoring the emergence of stripe patterns. These findings indicate that high curvature and strong confinement are critical factors in determining whether the system stabilizes into a stripe or hybrid configuration. In thinner shells, tilt degeneracy of the pitch axis results in extended regions with disordered stripes. In contrast, thicker shells provide sufficient space for the pitch axis to reorient, enabling the formation of distorted FCDs (Fig. 6C). As expected, for thin shells ($h \lesssim 1.5p$), the influence of the anchoring transition at the outer surface becomes more pronounced, facilitating the formation of a uniform stripe pattern (Fig. 6C).

In the second approach, we examined changes in anchoring energy, W, that could be induced by surfactant addition as a potential driving force for the observed configuration transition. We maintained planar anchoring on the outer surface while gradually reducing the anchoring energy from strong ($W \sim 1 \times 10^{-3}$ J m^{-2}) to weak ($W \sim 1 \times 10^{-5}$ J m^{-2}). At low anchoring energy, the CLC is no longer constrained to maintain a tangential orientation at the outer boundary, which can allow the emergence of patterns resembling those formed under homeotropic anchoring conditions. We achieved this by iteratively lowering W, allowing the system to relax between each reduction. This process enabled us to analyze the phase structure's response to small changes in the interface and identify potential transitions from the RSS to a stripe configuration. The results, shown in Fig. 7, reveal an abrupt change in the free energy density (f) when $W < 1 \times 10^{-4}$ J m^{-2}.

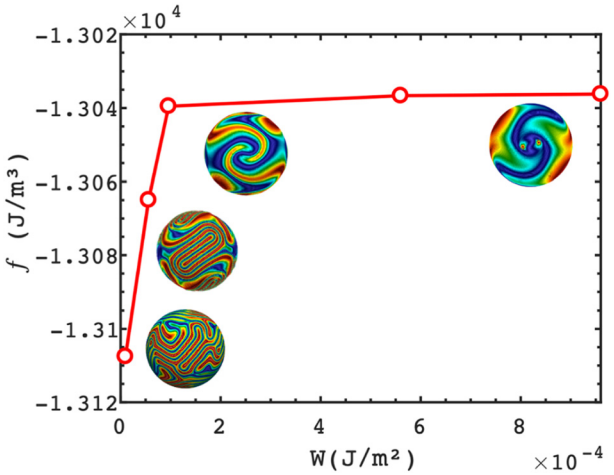

Fig. 7 Simulation results of free energy density for shells with planar anchoring on both surfaces. The anchoring energy of the inner surface is kept strong ($W = 1 \times 10^{-3}$ J m^{-2}), while the outer anchoring energy is lowering. An abrupt change takes place around ($W = 1 \times 10^{-4}$ J m^{-2}).

Notably, a stripe pattern emerges in the region where RSS defects were located, and additional stripe patterns form around the shell. These simulations suggest that FCDs can coexist with stripe patterns at moderate anchoring energies ($W \sim 5 \times 10^{-5}$ J m^{-2}).

These simulation results indicate that SDS promotes homeotropic anchoring more effectively than reducing planar anchoring energy, as a well-defined stripe pattern only formed under homeotropic anchoring conditions on the outer shell surface. Nevertheless, the simulations also reveal conditions that can induce significant structural changes in CLC shells by modifying their outer anchoring energy.

Taken together, these findings highlight the importance of shell's geometric scale in steering textural outcomes in highly chiral CLC shells undergoing anchoring transitions. As the shell thickness approaches just a few pitch lengths, traditional cholesteric texturing modes break down, giving way to complex, coexisting FCDs and stripe morphologies. The irregular and asymmetric nature of both FCDs and stripe domains highlights the fundamentally discrete and defect-mediated character of pattern formation dictated by extreme spatial frustration. These hybrid textures present compelling opportunities for modulating optical anisotropy and spatially encoding functionalities in reconfigurable chiral materials. Additionally, the dominance of stripe formation in small droplets under asymmetric anchoring reinforces the role of curvature as a design parameter for tailoring director configurations. The spatial coherence of these stripe patterns positions them as attractive candidates for templating anisotropic optical responses in microscale chiral materials, particularly where defect suppression is desirable for functional applications.

4. Conclusions

This work elucidates the complex interplay between curvature, shell thickness, and anchoring asymmetry in defining structural transitions and defect morphologies within highly chiral cholesteric liquid crystal (CLC) shells. By systematically modulating the boundary conditions from planar–planar to planar-homeotropic configurations and controlling confinement *via* shell geometry, we reveal a rich landscape of textural transformations characterized by FCD formation, stripe pattern stabilization, and hybrid states arising from geometric frustration.

Our experimental results demonstrate that thick shells facilitate pitch-axis reorientation through the nucleation and growth of FCDs, enabling elastic energy minimization *via* layer bending. In contrast, ultra-thin shells with increased confinement exhibit irregular, fragmented domain morphologies and stripe-like textures, indicative of incomplete elastic relaxation and metastable defect configurations. Furthermore, in small-diameter shells, curvature imposes an additional constraint, effectively suppressing FCD formation and favoring the emergence of periodic stripe patterns as an alternative structural motif. These findings highlight the pivotal role of curvature not only in modifying the local energy

landscape but also in stabilizing non-singular director configurations that are inaccessible in bulk geometries.

Continuum simulations based on the Landau–de Gennes framework corroborate experimental observations and provide insight into the energetic pathways of anchoring-induced transitions. The simulations reveal critical anchoring energy thresholds required to trigger reorientation, identify regimes of morphological coexistence, and confirm the stabilizing influence of homeotropic anchoring on stripe formation.

Collectively, these results advance our understanding of topological and geometrical control in chiral liquid crystalline systems and establish design principles for directing structural transitions in confined CLCs. This work provides a foundational framework for exploiting curvature and anchoring asymmetry to engineer responsive chiro-optical materials, programmable colloidal assemblies, and soft-matter devices with tailored anisotropic functionalities.

Conflicts of interest

The authors declare no competing financial interest.

Data availability

Supplementary information is available: The SI includes Movies S1 through S4, which demonstrate the dynamic structural transition from planar–planar to planar–homeotropic alignment under varying conditions of shell thickness and droplet size, corresponding to Fig. 2 through 5. See DOI: **https://doi.org/10.1039/D5ME00070J**.

All data supporting the findings of this study are available within the article. Additional datasets and simulation code used in this work are available from the corresponding author upon reasonable request.

Acknowledgements

This work has been supported by the National Science Foundation, Division of Materials Research, Condensed Matter Physics program, with the NSF CAREER award 2146428.

References

1 P.-G. De Gennes and J. Prost, *The physics of liquid crystals*, Oxford university press, 1993.
2 D. R. Nelson, *Defects and geometry in condensed matter physics*, Cambridge University Press, 2002.
3 A. Doostmohammadi and B. Ladoux, Physics of liquid crystals in cell biology, *Trends Cell Biol.*, 2022, **32**(2), 140–150, DOI: **10.1016/j.tcb.2021.09.012**.
4 A. D. Rey, Liquid crystal models of biological materials and processes, *Soft Matter*, 2010, **6**(15), 3402–3429, DOI: **10.1039/B921576J**.
5 T. B. Saw, A. Doostmohammadi, V. Nier, L. Kocgozlu, S. Thampi, Y. Toyama, P. Marcq, C. T. Lim, J. M. Yeomans and B. Ladoux, Topological defects in epithelia govern cell death and extrusion, *Nature*, 2017, **544**(7649), 212–216.
6 H. Coles and S. Morris, Liquid-crystal lasers, *Nat. Photonics*, 2010, **4**(10), 676–685, DOI: **10.1038/nphoton.2010.184**.
7 C. Bahr and H.-S. Kitzerow, *Chirality in liquid crystals*, Springer, 2001.
8 M. Sadati, Y. Zhou, D. Melchert, A. Guo, J. A. Martinez-Gonzalez, T. F. Roberts, R. Zhang and J. J. de Pablo, Spherical nematic shells with a prolate ellipsoidal core, *Soft Matter*, 2017, **13**(41), 7465–7472, DOI: **10.1039/C7SM01403A**.
9 M. Sadati, A. I. Apik, J. C. Armas-Perez, J. Martinez-Gonzalez, J. P. Hernandez-Ortiz, N. L. Abbott and J. J. de Pablo, Liquid Crystal Enabled Early Stage Detection of Beta Amyloid Formation on Lipid Monolayers, *Adv. Funct. Mater.*, 2015, **25**(38), 6050–6060, DOI: **10.1002/adfm.201502830**.
10 M. Rahimi, T. F. Roberts, J. C. Armas-Pérez, X. Wang, E. Bukusoglu, N. L. Abbott and J. J. de Pablo, Nanoparticle self-assembly at the interface of liquid crystal droplets, *Proc. Natl. Acad. Sci. U. S. A.*, 2015, **112**(17), 5297–5302, DOI: **10.1073/pnas.1422785112**.
11 J. A. Moreno-Razo, E. J. Sambriski, N. L. Abbott, J. P. Hernández-Ortiz and J. J. de Pablo, Liquid-crystal-mediated self-assembly at nanodroplet interfaces, *Nature*, 2012, **485**(7396), 86–89, DOI: **10.1038/nature11084**.
12 I.-H. Lin, D. S. Miller, P. J. Bertics, C. J. Murphy, J. J. de Pablo and N. L. Abbott, Endotoxin-induced structural transformations in liquid crystalline droplets, *Science*, 2011, **332**(6035), 1297–1300.
13 S. Norouzi, J. A. Martinez Gonzalez and M. Sadati, Chiral Liquid Crystal Microdroplets for Sensing Phospholipid Amphiphiles, *Biosensors*, 2022, **12**(5), 313.
14 D. A. Paterson, X. Du, P. Bao, A. A. Parry, S. A. Peyman, J. A. T. Sandoe, S. D. Evans, D. Luo, R. J. Bushby, J. C. Jones and H. F. Gleeson, Chiral nematic liquid crystal droplets as a basis for sensor systems, *Mol. Syst. Des. Eng.*, 2022, **7**(6), 607–621, DOI: **10.1039/D1ME00189B**.
15 M. Humar and I. Muševič, 3D microlasers from self-assembled cholesteric liquid-crystal microdroplets, *Opt. Express*, 2010, **18**(26), 26995–27003.
16 J. Yoshioka, F. Ito and Y. Tabe, Stability of a double twisted structure in spherical cholesteric droplets, *Soft Matter*, 2016, **12**(8), 2400–2407, DOI: **10.1039/C5SM02838H**.
17 Y. Zhou, E. Bukusoglu, J. A. Martínez-González, M. Rahimi, T. F. Roberts, R. Zhang, X. Wang, N. L. Abbott and J. J. de Pablo, Structural Transitions in Cholesteric Liquid Crystal Droplets, *ACS Nano*, 2016, **10**(7), 6484–6490, DOI: **10.1021/acsnano.6b01088**.
18 G. Posnjak, S. Čopar and I. Muševič, Points, skyrmions and torons in chiral nematic droplets, *Sci. Rep.*, 2016, **6**(1), 26361, DOI: **10.1038/srep26361**.
19 A. Darmon, M. Benzaquen, D. Seč, S. Čopar, O. Dauchot and T. Lopez-Leon, Waltzing route toward double-helix formation in cholesteric shells, *Proc. Natl. Acad. Sci. U. S. A.*, 2016, **113**(34), 9469–9474, DOI: **10.1073/pnas.1525059113**.
20 L. Tran, M. O. Lavrentovich, G. Durey, A. Darmon, M. F. Haase, N. Li, D. Lee, K. J. Stebe, R. D. Kamien and T. Lopez-Leon, Change in Stripes for Cholesteric Shells via Anchoring

in Moderation, *Phys. Rev. X*, 2017, **7**(4), 041029, DOI: **10.1103/PhysRevX.7.041029**.

21 G. Durey, H. R. O. Sohn, P. J. Ackerman, E. Brasselet, I. I. Smalyukh and T. Lopez-Leon, Topological solitons, cholesteric fingers and singular defect lines in Janus liquid crystal shells, *Soft Matter*, 2020, **16**(11), 2669–2682, DOI: **10.1039/C9SM02033K**.

22 S. S. Lee, H. J. Seo, Y. H. Kim and S.-H. Kim, Structural Color Palettes of Core–Shell Photonic Ink Capsules Containing Cholesteric Liquid Crystals, *Adv. Mater.*, 2017, **29**(23), 1606894, DOI: **10.1002/adma.201606894**.

23 Y. Geng, J.-H. Jang, K.-G. Noh, J. Noh, J. P. F. Lagerwall and S.-Y. Park, Through the Spherical Looking-Glass: Asymmetry Enables Multicolored Internal Reflection in Cholesteric Liquid Crystal Shells, *Adv. Opt. Mater.*, 2018, **6**(1), 1700923, DOI: **10.1002/adom.201700923**.

24 L. Tran and K. J. M. Bishop, Swelling Cholesteric Liquid Crystal Shells to Direct the Assembly of Particles at the Interface, *ACS Nano*, 2020, **14**(5), 5459–5467, DOI: **10.1021/acsnano.9b09441**.

25 S. Norouzi, A. Tavera-Vazquez, J. Ramirez-de Arellano, D. S. Kim, T. Lopez-Leon, J. J. de Pablo, J. A. Martinez-Gonzalez and M. Sadati, Elastic Instability of Cubic Blue Phase Nano Crystals in Curved Shells, *ACS Nano*, 2022, **16**(10), 15894–15906, DOI: **10.1021/acsnano.2c02799**.

26 M. Sadati, J. A. Martinez-Gonzalez, A. Cohen, S. Norouzi, O. Guzmán and J. J. de Pablo, Control of monodomain polymer-stabilized cuboidal nanocrystals of chiral nematics by confinement, *ACS Nano*, 2021, **15**(10), 15972–15981.

27 S.-W. Ko, S.-H. Huang, A. Y.-G. Fuh and T.-H. Lin, Measurement of helical twisting power based on axially symmetrical photo-aligned dye-doped liquid crystal film, *Opt. Express*, 2009, **17**(18), 15926–15931.

28 A. S. Utada, E. Lorenceau, D. R. Link, P. D. Kaplan, H. A. Stone and D. Weitz, Monodisperse double emulsions generated from a microcapillary device, *Science*, 2005, **308**(5721), 537–541.

29 S.-H. Kim, J.-G. Park, T. M. Choi, V. N. Manoharan and D. A. Weitz, Osmotic-pressure-controlled concentration of colloidal particles in thin-shelled capsules, *Nat. Commun.*, 2014, **5**(1), 3068.

30 M. Ravnik and S. Žumer, Landau–de Gennes modelling of nematic liquid crystal colloids, *Liq. Cryst.*, 2009, **36**(10–11), 1201–1214.

31 J. A. Martínez-González, Y. Zhou, M. Rahimi, E. Bukusoglu, N. L. Abbott and J. J. de Pablo, Blue-phase liquid crystal droplets, *Proc. Natl. Acad. Sci. U. S. A.*, 2015, **112**(43), 13195–13200.

32 M. Ravnik, J.-I. Fukuda, J. M. Yeomans and S. Žumer, Confining blue phase colloids to thin layers, *Soft Matter*, 2011, **7**(21), 10144–10150.

33 C. Denniston, Theory and simulation of objects in liquid crystals, *Adv. Phys.: X*, 2020, **5**(1), 1806728.

34 J. S. Lintuvuori, K. Stratford, M. Cates and D. Marenduzzo, Colloids in cholesterics: size-dependent defects and non-Stokesian microrheology, *Phys. Rev. Lett.*, 2010, **105**(17), 178302.

35 A. L. Hicks and S. W. Walker, Modelling and simulation of the cholesteric Landau-de Gennes model, *Proc. R. Soc. A*, 2024, **480**(2292), 20230813.

36 J.-B. Fournier and P. Galatola, Modeling planar degenerate wetting and anchoring in nematicliquid crystals, *Europhys. Lett.*, 2005, **72**(3), 403.

37 D. Seč, T. Porenta, M. Ravnik and S. Žumer, Geometrical frustration of chiral ordering in cholesteric droplets, *Soft Matter*, 2012, **8**(48), 11982–11988.

38 M. O. Lavrentovich and L. Tran, Undulation instabilities in cholesteric liquid crystals induced by anchoring transitions, *Phys. Rev. Res.*, 2020, **2**(2), 023128.